# Single-Crystalline Porous Hematite Nanorods: Photocatalytic and Magnetic Properties

Hyun Gil Cha,[†,§] Soo Jin Kim,[†,§] Kyu Joon Lee,[‡] Myung Hwa Jung,[‡] and Young Soo Kang[*,†]

[†]Korea Center for Artificial Photosynthesis, Department of Chemistry and [‡]Department of Physics, Sogang University, Seoul 121-742, Korea

S *Supporting Information*

ABSTRACT: Single-crystalline hematite nanorods with void pores were synthesized by a facile hydrothermal process and subsequent heat treatment in air. The pores were formed by removal of released H_2O in α-FeOOH nanorods and ionic liquids. The ionic liquids were adsorbed on the surface of O-terminated α-FeOOH nanorods by electrostatic force, and hydrogen bonds formed between the hydrogen atom at the C2 position of the imidazole ring and the oxygen atom of O−Fe. The proposed formation mechanism has been investigated on the basis of the TEM image and SAED pattern. Hematite with a different porosity and degree of crystallinity has a different photocatalytic property for the photodegradation of methyl orange. The temperature-dependent magnetization and magnetic hysteresis of samples indicate the interesting magnetic property evolution, which is attributed to the finite size and surface effect of the pore−solid architecture created by void pores in the rods.
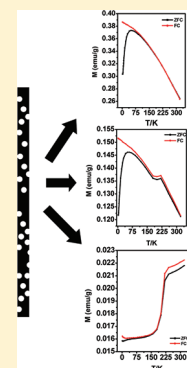
1. INTRODUCTION

Hollow and porous structures have been attracting great attention because of their widespread applications in catalysis, nanoelectronics, photonics, drug delivery, environmental engineering, lubrication, chemical storage, and sensor systems.[1−4] Diverse synthetic methods such as removal of the templating core,[5] galvanic replacement,[6] and the Kirkendall effect[7] have been developed to prepare these hollow nanoparticles.

Hematite (α-Fe$_2$O$_3$) has the corundum crystal structure and orders antiferromagnetically below its Neel temperature, $T_N \cong 961$ K. Bulk hematite has a Morin temperature of $T_M \cong 263$ K, below which the two sublattice spins aligned along the rhombohedral [111] axis are exactly antiparallel.[8] Above T_M the moments lie in the basal (111) plane with a slight canting away from the antiferromagnetic axis resulting in a small net magnetization in the plane. Hematite nanostructures have been widely studied with renewed interest in recent years because of their potential, due to the small intrinsic magnetic moment, for investigating the surface effect and magnetization reversal by quantum tunneling. Moreover, hematite with n-type semiconducting properties ($E_g = 2.1$ eV) under ambient conditions is of great scientific and technological importance.[9,10] Nanowires, nanorods, and nanotubes of Fe$_2$O$_3$ represent a class of 1D magnetic materials in which the motion of charge carriers is restricted in two directions so that they are expected to improve photochemical, photophysical, and electron-transport properties.[11]

We herein report that porous α-Fe$_2$O$_3$ nanorods have been prepared by a facile solution-phase approach. Sodium hydroxide and ionic liquid provides OH$^-$ at the rate of diffusion, and surfactants are used as templates to synthesize single-crystalline

α-FeOOH nanorods. They are then transformed into single-crystalline porous α-Fe$_2$O$_3$ nanorods with different porosity by heat treatment in air. In the present work, the magnetic properties are strongly dependent on the size of grains and void pores while the photocatalytic property is significantly dependent on the surface area.

2. EXPERIMENTAL SECTION

Material Preparation. Iron chloride hexahydrate (98%, Aldrich), sodium hydroxide (93%, Duksan, Korea), 1-butyl-3-methylimidazolium chloride (98%, C-TRI, Korea), and potassium bromide (FT-IR grade, >99%, Aldrich) were obtained from commercial sources. All chemicals were generally regent grade and used without further purification.

Single-crystalline porous α-Fe$_2$O$_3$ nanorods were synthesized via a solution chemical route involving two steps. (1) Synthesis of single-crystalline α-FeOOH nanorods: 2 mmol of FeCl$_3$·6H$_2$O and 2 mmol of NaOH were put into 20 mL of deionized water under stirring to form a homogeneous solution. Subsequently, 6 mmol of the ionic liquid of 1-n-butyl-3-methylimidazolium chloride ([BMIM][Cl]) was added into the above solution under continuous stirring. After stirring for 20 min, the solution was transferred into a Teflon-lined stainless-steel autoclave with a capacity of 23 mL, sealed, and heated at 423 K for 6 h without shaking or stirring during the reaction time. When the reaction

Table 1. Synthetic Condition and BET Data for Different α-Fe₂O₃ Nanoporous Rods

sample	grain size (nm)	pore diameter (nm)	surface area (m²/g)	reaction condition for Fe₂O₃, K
S1	12	2.441	96.73	523
S2	21	5.325	33.26	623
S3	23	6.737	27.28	673

was completed, the autoclave was cooled to room temperature naturally. The resultant product was collected and washed with deionized water and anhydrous ethanol several times until the solution was neutral. The final red product was dried in a vacuum at 353 K for 3 h. (2) Transformation from single-crystalline α-FeOOH nanorods to single-crystalline porous α-Fe₂O₃ nanorods: The single-crystalline porous α-Fe₂O₃ nanorods were obtained by heating the as-prepared α-FeOOH nanorods in air at 523, 623, 673, and 723 K for 3 h, preserving the same rodlike morphology. The prepared samples are summarized in Table 1, where the obtained porous α-Fe₂O₃ nanorods have been named as S1, S2, and S3. The collected solid products were washed with ethanol and distilled water several times and then dried in a vacuum at 333 K for 4 h.

Materials Characterization. Scanning electron microscopy (SEM) images were obtained using a field-effect scanning electron microscope (Hitachi S-4300) operated at an acceleration voltage of 20 kV. A platinum/palladium alloy (in a ratio of 8 to 2) with a thickness of about 15 nm was deposited on top of the samples. Transmission electron microscope (TEM, JEM 2100F) images, selected area electron diffraction (SAED), and chemical composition were obtained from a JEOL transmission electron microscope (JEM 2100F) installed with an energy-dispersive X-ray (EDX) operated at accelerating 200 keV. In these HRTEM experiments, the electron beam was incident along the direction perpendicular to the 1D nanostructure. The nanostructures were transferred onto TEM copper grids by sonicating the substrate in alcohol following dipping the grids into the solution. EDX line scans were obtained using an Oxford Horiba EX-220 Energy Dispersive X-ray Micro Analyzer (model 6853-H). Powder X-ray diffraction (XRD) patterns were obtained using a Rigaku D/MAX-2500/pc diffractometer. Thermogravimetric analysis (TGA) and differential scanning calorimetry (DSC) data were collected from room temperature to 600 °C at a heating rate of 10 °C using a SINCO, STA-1500 analyzer. Measurement of the IR spectrum was performed on Thermo Nicolet avatar 330 FT-IR applying the KBr pellet technique, with 8 cm⁻¹ resolution over a scanning range of 400−4000 cm⁻¹. Diffuse-reflectance UV−vis spectra of the powder samples was recorded on a Varian Cary 5000 UV−vis spectrophotometer equipped with an integrating sphere. Barium sulfate was used as the reference. The diffuse reflectance spectra were converted into the Kubelka−Munk (K−M) formalism. Specific surface areas of the samples were obtained using N₂ adsorption−desorption at 77.3 K in Quantachrome Autosorb-1. Prior to N₂ adsorption, the samples were thermally pretreated at 100 °C under vacuum for (3 × 10⁻⁵ Torr) for 10 h. Magnetic measurements were carried out with a Quantum Design SQUID-VSM dc magnetometer. The hysteresis was recorded for powdered samples of porous hematite nanorods in a gelatin capsule. The temperature was varied between 5 and 350 K according to a zero-field cooling (ZFC) and field cooling (FC) procedure at 1 kOe, and the hysteretic loops were obtained in a magnetic field up to +3 to −3 kOe.
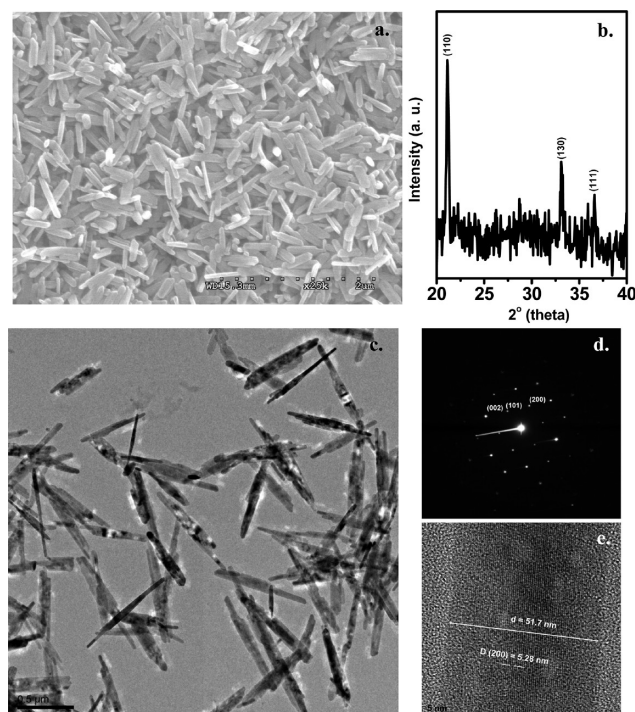

Figure 1. SEM image (a), XRD pattern (b), TEM image (c), SAED pattern (d), and HRTEM image (e) of α-FeOOH nanorods at 423 K for 6 h.

Photoreactivity Measurement. The photocatalytic property of porous α-Fe₂O₃ nanorods was measured by the photodegradation of methyl orange solution, which was selected as a standard sample. A 30 mg amount of each porous nanorod with different pore size and crystallinity was added to 30 mL of 1.25 × 10⁻⁵ mol/L aqueous methyl orange solution. Prior to irradiation, the suspensions were magnetically stirred in the dark for 30 min to establish the adsorption/desorption equilibrium between the dye and the porous α-Fe₂O₃ nanorods. Subsequently, 0.15 mL of H₂O₂ (3%) was added into the mixed solution. The mixed solution was then transferred into a 50 mL quartz test tube and irradiated with a solar simulator (AM1.5, 1 sun) at a distance of about 15 cm. At given irradiation time intervals, 5 mL samples were withdrawn from the test tube for analysis. The absorption spectra of these solutions were taken with a Shimadzu UV-310PC spectrophotometer.

3. RESULTS AND DISCUSSION

Figure 1a shows a typical SEM image of the prepared α-FeOOH nanorods. It can be clearly seen that α-FeOOH rodlike features with an average length of 48−83 nm and a mean diameter of 340−850 nm are obtained on a large scale. As shown in Figure 1b, all XRD patterns can be indexed as orthorhombic α-FeOOH with unit cell constants of a = 0.4592 nm, b = 0.998 nm, and c = 0.3015 nm, which is consistent with the reported data (JCPDS card no. 81-0464).[12] The fine structure of samples in Figure 1d and 1e was further characterized by the HRTEM image and SAED pattern. The TEM image in Figure 1c shows that the rods can be clearly observed in all the visible nanorods with a 50−65 nm diameter and 560−790 nm length. The SAED pattern further verifies the single-crystalline nature of the nanorod in order to distinguish the existence of different domains that
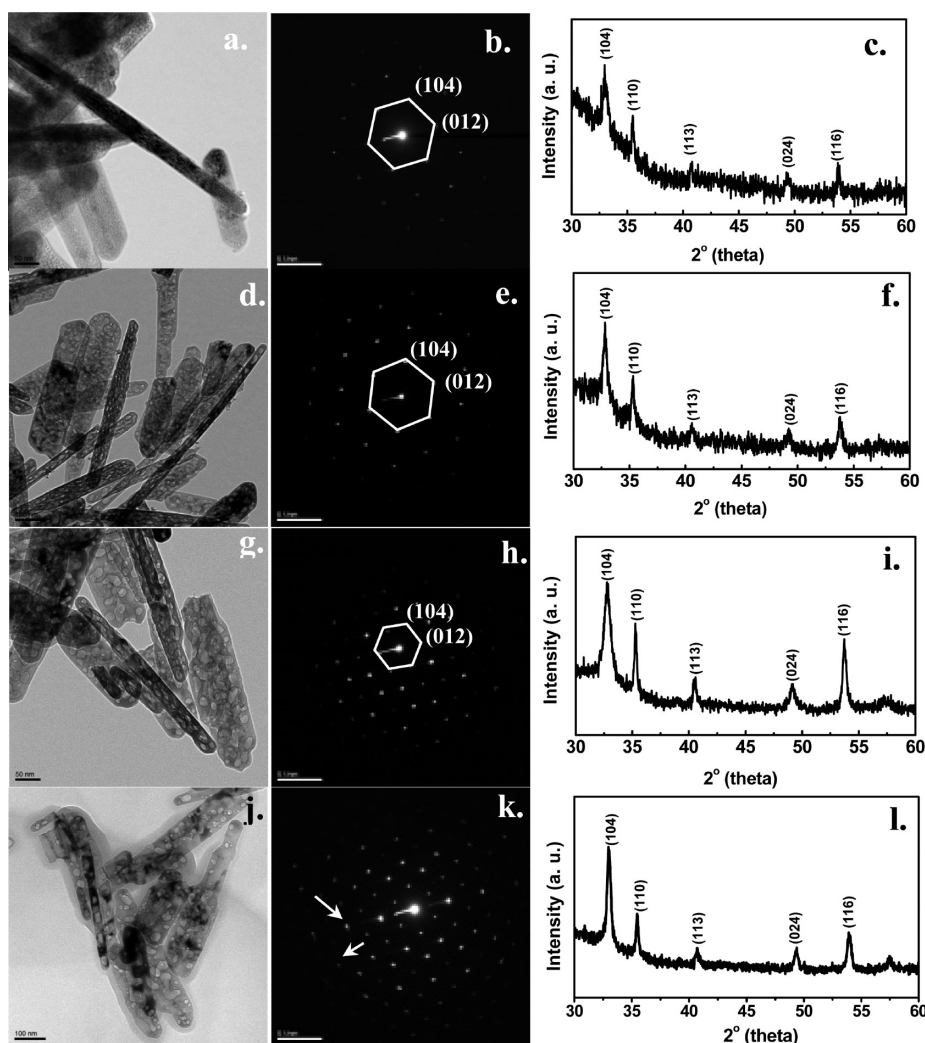
Figure 2. Representative TEM images and SAED patterns of the porous α-Fe$_2$O$_3$ nanorods with different pore size for S1 (a and b), S2 (d and e), S3 (g and h), S4 (j and k) prepared by heat treatment of α-FeOOH nanorods at 523, 623, 673, and 723 K for 3 h in air. The corresponding XRD patterns for the samples of S1, S2, S3, and S4 are shown in panels c, f, i, and l, respectively.

could indicate the presence of different polytypes or disorder along the structure in Figure 1d. However, the whole crystal seems to be homogeneous, and only the maxima corresponding to the above-described unit cell are observed. As shown in Figure 1e, a HRTEM image of a single-crystalline nanorod showing the clear interplanar distance 5.28 Å matches well with the d_{200} spacing of pure α-FeOOH. This suggests that growth occurs along the rod, toward the [200] direction. The clear constant lattice fringes indicate that each rod is single crystalline in nature.

The chemical structure of ionic liquid and TGA-DSC plots of the synthesized samples are shown (see Figure S1, Supporting Information). TGA and DSC studies have been carried out for porous nanorods with adsorbed [BMIM].$^+$ The weight loss of product is slowly increased up to 473 K due to evaporation of adsorbed water and dehydroxylation of α-FeOOH/[BMIM]. An exothermal peak at 245 K can be seen in the DSC plots, which is indicative of the structure transformation of α-FeOOH to α-Fe$_2$O$_3$, and a strong sharp peak at 573 K represents the weight loss accounted for by the [BMIM]$^+$ cation. The broad shoulders in the range of 583–873 K may be attributed to loss of the

[BMIM]$^+$ adsorbed on the surface of the O$_2$-terminated surface of α-FeOOH and sufficient oxide in the hybrid material, which is consistent with the calculated result (32.6 wt %) based on the conversion of [FeOOH][BMIM]$^+$ to α-Fe$_2$O$_3$ (JCPDS no. 33-0664).[13] Thermal decomposition of this hybrid with increasing temperature from 518 to 873 K results in formation of pure α-Fe$_2$O$_3$ inorganic phase, which is confirmed by the XRD pattern in Figure 2c, 2f, 2i, and 2l.

Further evidence for the formation of the α-FeOOH can be obtained from the FT-IR spectrum of the sample as shown (see Figure S2, Supporting Information). The strong peaks at 3120, 892, 791, and 628 cm^{-1} are the characteristic vibrations in the α-FeOOH product. These peaks disappear and two new strong absorption peaks are observed after heat treatment at different temperatures. The peaks at 545 and 470 cm^{-1} are assigned to Fe–O characteristic vibrations of α-Fe$_2$O$_3$, indicating formation of the α-Fe$_2$O$_3$ phase (see Figure S2b–e, Supporting Information). As described above, the systems with addition of ionic liquid retained the morphology of the α-FeOOH precursors after transformation to α-Fe$_2$O$_3$ and have regular pores after removal of ionic liquid and thermal dehydration by heat treatment in air.[14]
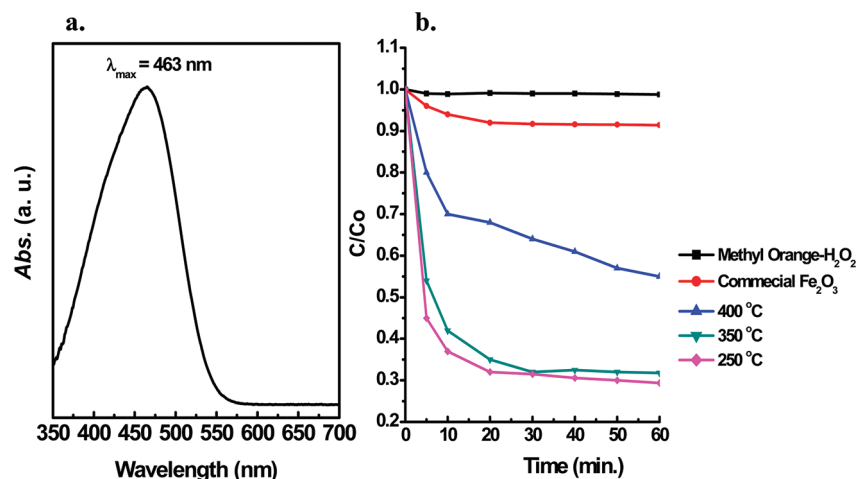
Figure 3. (a) Absorption spectrum of methyl orange−H_2O_2 solution; (b) fitting of the absorbance maximum plot vs photoirradaition times with a solar simulated light source (AM1.5, 1 Sun) for photodegradated methyl orange−H_2O_2 solution containing commercial α-Fe_2O_3 nanoparticles and α-Fe_2O_3 porous nanorods with different pore sizes.

Figure 2 shows that when heat treated the product prepared from α-FeOOH nanorods yielded the porous α-Fe_2O_3 nanorods with altered morphology of the 1D and even the nanorod bundles, and many pores with diameter of 2−8 nm are formed in the nanorods. The TEM images in Figure 2a, 2d, 2g, and 2j show that samples (S1−S4) were solid and smoothly rod shaped with diameters of 48−83 nm and lengths of 340−850 nm. The SAED patterns of the heat-treated α-FeOOH nanorods at different temperatures given in Figure 2b, 2e, 2h, and 2k are consistent with the rhombohedral structure featuring strong patterns assigned to the (104), (110), and (116) planes. As heating temperature is increased, the intensity of those peaks and pore sizes were increased. However, the single-crystal pattern of the obtained product in the SAED pattern of S4 is slightly disordered. It means that the crystal structure of single-crystallized porous α-Fe_2O_3 nanorods (single-domain) was gradually changed to polycrystallized porous nanorods (multidomain) because of the relatively high heating temperature and pore size growth.[15]

The purity and crystallinity of as-prepared samples were examined using powder XRD measurement as shown in Figure 2c, 2f, 2i, and 2l. The XRD patterns of the as-prepared Fe_2O_3 porous nanorods were obtained by heat treatment of as prepared α-FeOOH nanorods in air at different temperatures (523, 623, 673, and 723 K) for 3 h, respectively. It is evident that all of the expected peaks can be indexed to the rhombohedral structure α-Fe_2O_3 (space group $R3c$, No. 167) with structural parameters of $a = b = 5.035$ Å, $c = 13.74$ Å, $\alpha = \beta = 90°$, and $\gamma = 120°$, which are in agreement with the literature, i.e., JCPDS card 33-0664. No characteristic peak was observed for other impurities such as α-FeOOH, Fe_3O_4, and γ-Fe_2O_3 and other metal ions.

According to the full width at half-maximum (fwhm) of the diffraction peaks, the average crystallite grain size of the obtained porous nanorods can be estimated from the Scherrer equation[16] to be summarized in Table 1

$$D_{hkl} = K\lambda/(\beta_{hkl}\cos\theta_{hkl})$$

where D_{hkl} is the particle size perpendicular to the normal line of the (hkl) plane, K is a constant (it is 0.9), β_{hkl} is the full width at

half-maximum of the (hkl) diffraction peak, θ_{hkl} is the Bragg angle of the (hkl) peak, and λ is the wavelength of the X-ray. On the basis of the above results, it is only concerned with the single-crystalline porous α-Fe_2O_3 nanorods (S1−S3).

Hematite nanomaterials have been used widely as ultraviolet absorbents for their broad absorption in the ultraviolet region from the electronic transition of Fe−O. Figure S3, Supporting Information, shows the optical absorbance spectra of the porous hematite nanorods (S1−S3) with photon energy in the range of 200−800 nm. It reveals two absorption edges around 300−600 and 600−750 nm for all samples, which carries two additional edges around 350 and 660 nm (see Figure S3, Supporting Information).

It is established[17] that three types of electronic transitions occur in the optical absorption spectra of Fe^{3+} substance: (a) the Fe^{3+} ligand field transition or the d−d transition, (b) the ligand to metal charge-transfer transition, and (c) the pair excitation resulting from simultaneous excitations of two neighboring Fe^{3+} cations that are magnetically coupled. Therefore, the absorption edge in the region from 400 to 600 nm (thus including the observed edge to around 540−560 nm) can be assigned to the $^6A_1 \rightarrow {}^4T_2$ (^4G) ligand field transition of Fe^{3+} as well as to the pair excitation processes $^6A_1 + {}^6A_1 \rightarrow {}^4T_2$ (^4G) + $^4T_2$ (^4G) transition of two adjacent Fe^{3+} centers ($^6A_1$ and $^4T_2$ (^4G)), referred to as the ground state and the first excited state configuration of the high-spin Fe^{3+}, respectively. Absorption bands near 430 and 390 nm correspond to the $^6A_1 \rightarrow$ 4E, $^4A_1$ (^4G) and $^6A_1 \rightarrow {}^4E$ (^4G) ligand field transition of Fe^{3+}. The region from 600 to 750 nm can be assigned to the $^6A_1 \rightarrow {}^4T_2$ (^4D) transition at about 670−680 nm. Additionally, in the region from 360 to 380 nm the absorption mainly results from the ligand to metal charge-transfer transitions and partially from the contributions of the Fe^{3+} ligand field transition $^6A_1 \rightarrow {}^4T_2$ (^4D). As the UV−vis spectra (see Figure S3, Supporting Information) reveal the electronic transition for the charge transfer or the pair excitation process in the wavelength region 300−600 nm is much more intense compared with those for ligand field transitions in the region of 600−750 nm, indicating a larger probability of the transition in the former case due to the selection rule. The reported band edge of the Fe_2O_3 samples is located at 2.1 eV, which is close to our obtained value of 2.17−2.23 eV. This

19132

dx.doi.org/10.1021/jp206958g |*J. Phys. Chem. C* 2011, 115, 19129−19135

transition in this energy region includes the d−d transition, pair excitations, and less charge transfer. The results indicate that the crystallinity and pore size of the samples have a large influence on their optical properties.

The hollow nature of the products was further confirmed by measurement of the pore size distribution, which was obtained by the nitrogen adsorption−desorption isotherm and Barret−Joyner−Halenda (BJH) methods.[18] In Table 1, the Brunauer−Emmett−Teller (BET) surface area of the as-obtained nanorods was found to be 96.73, 33.26, and 27.28 m^2/g by calculating from the results of N_2 adsorption. Considering the factors that affect specific surface area, we can conclude that, in a comparable size range, it is the pores that increase specific area, whereas when there is a wide size discrepancy it is the size that determines the specific surface area. It is worth noting that the as-obtained porous α-Fe_2O_3 nanorods with the gradient in pore size and particle size provide a fine example to study the size-dependent property of magnetism. BJH analysis showed that the Fe_2O_3 porous nanorods possessed a multimodal mesoporous distribution with increasing heating temperature. The various pore size distributions in the as-obtained nanorods are displayed (see the inset of Figure S4b and S4c, Supporting Information). Because of its porous structure, we expect the obtained nanorods to be useful as photocatalyst. To evaluate the photocatalytic activity of our product, herein, we used commercial Fe_2O_3 nanoparticle and the as-prepared porous nanorods. Methyl orange (MO) was selected as the model organic pollutant. The initial concentration of the MO solution was set to be 20 mg/L. The absorbance spectrum of MO is recorded in Figure 3a. UV−vis absorption spectroscopy was used to record the adsorption behavior of the solution after treatment. Figure 3b shows the evolution of MO absorption spectra in the presence of 40 mg of α-Fe_2O_3 porous nanorods. The characteristic light absorption process can be divided into two stages. In the first stage, MO was immediately adsorbed within 10 min ($C/C_0 = 0.38$), and in the following second stage from 10 to 60 min, MO molecules were adsorbed steadily ($C/C_0 = 0.3$). The removal capacity of the porous nanorods was calculated to be 34.5 mg/g. Removal of MO may be associated with the electrostatic attraction between the iron oxide surface and the MO molecule. For a comparison, commercial α-Fe_2O_3 was also used to remove MO in solution. As shown by the red line in Figure 3b, the commercial α-Fe_2O_3 showed much lower efficiency in removing MO. The favorable performance could be attributed to the highly porous structure and high surface area of the as-prepared sample.[19] From the above-mentioned results, due to different porosity and crystallinity, the prepared α-Fe_2O_3 porous nanorods would be highly promising candidates to be applied as photocatalysts for environmental protection.

It is generally accepted that the magnetic properties of nanoscaled materials are highly sensitive to the size, morphology, and crystal structure including defects and substitutions. Nanoscaled materials often exhibit unusual behaviors, which are different from those of bulk materials, owing to the shape- and size-dependent effects. It is of great interest to investigate the magnetic properties of α-Fe_2O_3 with different porosity and grain size.

It has been reported that bulk α-Fe_2O_3 shows an antiferromagnetic (AFM) transition at the Neel temperature (T_N = 961 K),[20] followed by a Morin transition (T_M) at 263 K.[21] The antiferromagnetically aligned spins are slightly canted spins, which gives rise to a weakly ferromagnetic (FM) moment below
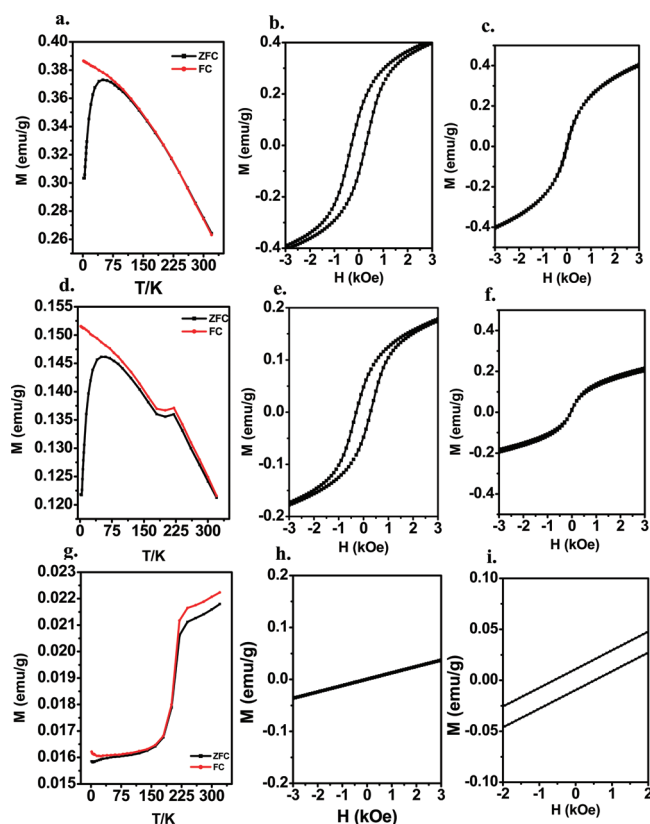
Figure 4. Magnetic properties of samples S1 (a−c), S2 (d−f), and S3 (g−i): temperature dependence of ZFC and FC magnetization at 1 kOe (a, d, g) and magnetic-field dependence of magnetization measured at 5 (b, e, h) and 300 K (c, f, i).

T_N. Then, the magnetic moments are completely ordered in AFM form below T_M, where there is no net magnetization. On the other hand, T_M of α-Fe_2O_3 nanorods with nanoscaled material is strongly suppressed by reducing the size. This indicates that the surface spins play an important role in the magnetic properties. In this sense, we measured the temperature dependence of magnetization for porous α-Fe_2O_3 nanorods with different grain sizes and pore sizes in Figure 4. In the case of S3, we observed the Morin temperature at 200 K in Figure 4g, which is lower than that (T_M = 263 K) for bulk α-Fe_2O_3. Thus, we conclude that the lower size with a large surface area is sufficient to suppress the Morin temperature. This result is in good agreement with previously reported studies.[21] As indicated in Table 1, the surface area of S3 is about 27 m^2/g. With increasing surface area (i.e., reduced the grain size) for S2, the Morin temperature is almost smeared out but instead a new anomaly takes place around T_B = 50 K. On further increasing the surface area for S1, the Morin transition disappears in Figure 4a. The ZFC curve shows a cusp at 50 K, while the FC curve monotonically increases on cooling. This deviation between ZFC and FC is most likely associated with the superparamagnetic behavior with spontaneous magnetization. The temperature where the ZFC curve shows a cusp is characterized as a blocking temperature (T_B). This blocking temperature is manifested in the $M-T$ curves. As shown in Figure 4, we observed the hysteresis with the coercive field (H_c) at 5 K between S1 (Figure 4 b) and S2 (Figure 4 e) and no hysteresis at 300 K (Figure 4c and 4f) above T_B. It should be noted that the FM component is more enhanced

19133

dx.doi.org/10.1021/jp206958g |*J. Phys. Chem. C* 2011, 115, 19129−19135
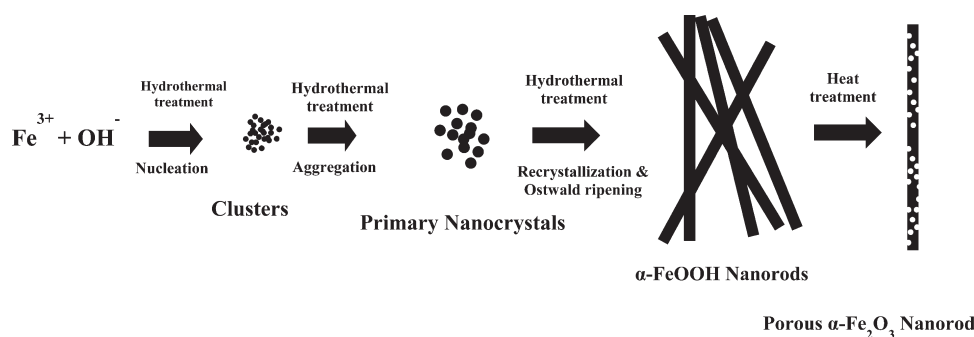
Figure 5. Schematic illustration for the formation mechanism of porous α-Fe$_2$O$_3$ nanorods with various void pore sizes at different heat-treatment temperatures.

with increasing surface area because of the spontaneous FM signal of the surface spins in addition to the uncompensated weak ferromagnetic signal of canted α-Fe$_2$O$_3$ spins.

Figure 5 shows a schematic illustration of the growth of α-FeOOH nanorods and crystal transformation from α-FeOOH nanorods to porous α-Fe$_2$O$_3$ nanorods. On the basis of the experimental results, the possible reaction mechanism in the NaOH system may be illustrated as follows

$$Fe^{3+} + OH^- \rightarrow Fe(OH)_3 \tag{1}$$

$$Fe(OH)_3 \rightarrow FeOOH \tag{2}$$

As shown above, Fe^{3+} reacted with the OH^- which was produced by hydrolysis of $Fe(OH)_3$ to form the yellow α-FeOOH suspension. Formation of solid-phase α-FeOOH in reaction 2 was confirmed with XRD measurement in Figure 2. In principle, the crystal growth process in solution mainly consists of nucleation and growth, which is affected by the intrinsic crystal structure and the external conditions including the kinetic energy barrier, temperature, time, capping molecules, and so forth. Formation of nanostructures after nucleation in solution relates to two primary mechanisms: the aggregation growth process and the Ostwald ripening process. Crystal growth by aggregation can occur by random aggregation and oriented aggregation, and the Oswald ripening process involves growth of larger crystals at the expense of smaller ones. In addition, the presence of [BMIM][Cl] was believed to play a strategic role in formation of this unique self-assembled superstructure as a soft template and a capping agent due to the important advantage of [BMIM]$^+$ which can form extended hydrogen-bond systems in the liquid state and are therefore highly structured. Previous studies by another group have demonstrated the synthesis of nanostructures by the ionic liquid-assisted route and the hydrogen bond co-π–π stack mechanism.[22] The cations of ionic liquids can be easily adsorbed on the surface of the O$_2$-terminated surface by electrostatic force, and the hydrogen bond, formed between the hydrogen atom at the C2 position of the imidazole ring and the oxygen atoms of O–Fe, may act as an effective bridge to connect the O$_2$-terminated plane of the produced nuclei of metal oxide and cations of ionic liquid. The [BMIM]$^+$ cations will be aligned to facilitate the proposed relocation of the molecules based on its ability to self-assemble into ordered structures stabilized by additional π–π interactions between the imidazolium rings of [BMIM][Cl], thus resulting in the self-organization of the nanoparticles into the desired superstructures. To confirm the

above, FTIR spectra of pure [BMIM][Cl], FeOOH, and heat-treated samples were performed (see Figure S2, Supporting Information). The absorption bands at 3151 and 3093 cm^{-1} assigned to the stretching vibration of C2–H in an imidazole ring[23] become broadened and weakened after α-FeOOH is obtained in [BMIM][Cl]. The results above indicate that there are strong interactions between ionic liquids and the α-FeOOH in the form of the strong hydrogen bonds between the C2 ([BMIM]Cl) and O atom of α-FeOOH. Also, the change of the peak of the C–N stretching vibration (ν_{C-N}) mode of the imidazolium ring at 1019 cm^{-1} in the spectra in Figure S2a and S2b, Supporting Information, is an effective tool to examine the π–π stack of the imidazolium ring.[24] In the present case, it is easy to observe that the ν_{C-N} mode in curve b becomes broadened and weakened compared with the curve a. In addition, the ν_{C-N} mode of C–H of the alkyl chain of [BMIM]$^+$ around 2965 and 2872 cm^{-1} in curve b is also found to be influenced by the mutual packing. The observed variation of the ν_{C-H} mode of the alkyl chain can be explained in that the π–π-stacking interaction of the imidazolium ring may influence the nitrogen–alkyl carbon bond, changing the ν_{C-H} mode. Moreover, compared with that of S1, S2, and S3 as shown (see Figure S2c–e, Supporting Information), the Fe–O characteristic vibrations of the porous α-Fe$_2$O$_3$ nanorods are 556 and 447 cm^{-1}; the unique frequencies of the ionic liquid disappeared after heat treatment in air. According to the discussion above and the literature,[23–25] the proposed mechanism of void pore formation in hematite nanorod by release of water molecules and removing ionic liquid in the single-crystalline hematite nanorods is responsible.

4. CONCLUSION

We prepared single-crystalline porous hematite nanorods from α-FeOOH nanorods, surprisingly, by different heat treatments in air. The pore is formed by removal of released H$_2$O in α-FeOOH nanorods and ionic liquid, which adsorbed on the surface of O-terminated α-FeOOH nanorods, by electrostatic force and hydrogen bond formed between the hydrogen atom at C2 position of the imidazole ring and the oxygen atom of O–Fe. Even though the shapes of the porous hematite nanorods were completely retained during conversion, the pore and grain size of those were increased due to increasing heat treatment in air, while surface areas of each nanorod were reduced. The magnetic hysteresis measurements result in interesting behavior such as canted ferromagnetism and superparamagnetism. Also, the test of the photocatalytic property shows different results from those expected because the photocatalytic property was significantly

19134

dx.doi.org/10.1021/jp206958g |*J. Phys. Chem. C* 2011, 115, 19129–19135

dependent on the surface area. Owing to the facile method in preparing various pore and grain sizes of porous hematite nanorods, it is expected to be applicable to other fields, for example, sensor, magnetic sensors, catalytic fields, hydrogen storage, etc.

■ ASSOCIATED CONTENT

⑤ Supporting Information. TGA-DSC curve, FT-IR spectra, UV–vis spectra, and BET results. This material is available free of charge via the Internet at http://pubs.acs.org.

■ AUTHOR INFORMATION

Corresponding Author
*E-mail: yskang@sogang.ac.kr.

Author Contributions
§These authors contributed equally.

■ ACKNOWLEDGMENT

■ REFERENCES

(1) (a) Dinsmore, A. D.; Hsu, M. F.; Nikolaides, M. G.; Marquez, M.; Bausch, A. R.; Weitz, D. A. *Science* **2002**, *298*, 1006. (b) Li, G.; Liu, M.; Kou, H. Z. *Chem.—Eur. J.* **2011**, *17*, 4323.

(2) Park, S.; Lim, J. H.; Chung, S. W.; Mirkin, C. A. *Science* **2004**, *303*, 348.

(3) Ryan, J. V.; Berry, A. D.; Anderson, M. L.; Long, J. W.; Stroud, R. M.; Cepak, V. M.; Browning, V. M.; Rolison, D. R.; Merzbacher, C. I. *Nature* **2000**, *406*, 169.

(4) Maji, T. K.; Matsuda, R.; Kitagawa, S. *Nat. Mater.* **2007**, *6*, 142.

(5) Kim, S. −W.; Kim, M.; Lee, W. Y.; Hyeon, T. *J. Am. Chem. Soc.* **2005**, *127*, 2368.

(6) Sun, Y.; Mayers, B.; Xia, Y. *Adv. Mater.* **2003**, *15*, 641.

(7) Yin, Y.; Rioux, R. M.; Erdonmez, C. K.; Hughes, S.; Somorjai, G. A.; Alivisatos, A. P. *Science* **2004**, *304*, 711.

(8) Hansen, M. F.; Koch, C. B.; Mørup, S. *Phys. Rev. B* **2000**, *62*, 1124.

(9) Alivisatos, A. P. *Science* **1996**, *271*, 933.

(10) Henglein, A. *Chem. Rev.* **1989**, *89*, 1861.

(11) Cha, H. G.; Song, J.; Kim, H. S.; Shin, W.; Yoon, K. B.; Kang, Y. S. *Chem. Commun.* **2011**, *47*, 2441.

(12) Zeng, S.; Tang, K.; Li, T. *J. Colloid Interface Sci.* **2007**, *312*, 513.

(13) Liu, L.; Kou, H. Z.; Mo, W.; Liu, H.; Wang, Y. *J. Phys. Chem. B* **2006**, *110*, 15218.

(14) (a) Li, Y. G.; Tan, B.; Wu, Y. Y. *J. Am. Chem. Soc.* **2006**, *128*, 14258. (b) Li, Y. G.; Tan, B.; Wu, Y. Y. *Chem. Mater.* **2008**, *20*, 2602.

(15) Yang, S. C.; Yang, D. J.; Kim, J.; Hong, J. M.; Kim, H. G.; Kim, I. D.; Lee, H. *Adv. Mater.* **2008**, *20*, 1059.

(16) Han, Y. C.; Cha, H. G.; Kim, C. W.; Kim, Y. H.; Kang, Y. S. *J. Phys. Chem. C* **2007**, *111*, 6275.

(17) He, Y. P.; Miao, Y. M.; Li, C. R.; Wang, S. Q.; Cao, L.; Xie, S. S.; Yang, G. Z.; Zou, B. S.; Burda, C. *Phys. Rev. B* **2005**, *71*, 125411.

(18) Wu, N. L.; Wang, Z. Y.; Rusakova, I. A. *Science* **1999**, *285*, 1375.

(19) Amano, F.; Nogami, K.; Tanaka, M.; Ohtani, B. *Langmuir* **2010**, *26*, 7174.

(20) Gronvold, F.; Samuelsen, E. J. *J. Phys. Chem. Solids* **1975**, *36*, 249.

(21) Morin, F. *J. Phys. Rev.* **1950**, *78*, 819.

(22) (a) Zheng, W. J.; Liu, X. D.; Yan, Z. Y.; Zhu, L. J. *ACS Nano* **2009**, *3*, 115. (b) Wang, L.; Chang, L. X.; Zhao, B.; Yuan, Z. Y.; Shao, G. S.; Zheng, W. J. *Inorg. Chem.* **2008**, *47*, 1443. (c) Lian, J.; Duan, X.; Ma, J.; Peng, P.; Kim, T.; Zheng, W. J. *ACS Nano* **2009**, *3*, 3749.

(23) (a) Zhou, Y.; Schattka, J. H.; Antonietti, M. *Nano Lett.* **2004**, *4*, 477. (b) Lian, J. B.; Kim, D.; Liu, X. D.; Ma, J. M.; Zheng, W. J. *J. Phys. Chem. C* **2009**, *113*, 9135.

(24) Wang, L.; Chang, L.; Zhao, B.; Yuan, Z.; Shao, G.; Zheng, W. *Inorg. Chem.* **2008**, *47*, 1443.

(25) (a) Zheng, W. J.; Liu, X. D.; Yan, Z. Y.; Zhu, L. J. *ACS Nano* **2009**, *3*, 115. (b) Wang, L.; Chang, L. X.; Zhao, B.; Yuan, Z. Y.; Shao, G. S.; Zheng, W. J. *Inorg. Chem.* **2008**, *47*, 1443. (c) Zhu, J. M.; Shen, Y. H.; Xie, A. J.; Qiu, L. G.; Zhang, Q.; Zhang, S. Y. *J. Phys. Chem. C* **2007**, *111*, 7629.